Icarus 281 (2017) 19–31

Contents lists available at ScienceDirect

Icarus

journal homepage: www.elsevier.com/locate/icarus

Ices on Mercury: Chemistry of volatiles in permanently cold areas of Mercury's north polar region

M.L. Delitsky[a,*], D.A. Paige[b], M.A. Siegler[c], E.R. Harju[b,f], D. Schriver[b], R.E. Johnson[d], P. Travnicek[e]

[a] California Specialty Engineering, Pasadena, CA
[b] Dept of Earth, Planetary and Space Sciences, University of California, Los Angeles, CA
[c] Planetary Science Institute, Tucson, AZ
[d] Dept of Engineering Physics, University of Virginia, Charlottesville, VA
[e] Space Sciences Laboratory, University of California, Berkeley, CA
[f] Pasadena City College, Pasadena, CA

ARTICLE INFO

Article history:
Received 3 January 2016
Revised 29 July 2016
Accepted 2 August 2016
Available online 4 August 2016

Keywords:
Mercury surface ices magnetospheres radiolysis

ABSTRACT

Observations by the MESSENGER spacecraft during its flyby and orbital observations of Mercury in 2008–2015 indicated the presence of cold icy materials hiding in permanently-shadowed craters in Mercury's north polar region. These icy condensed volatiles are thought to be composed of water ice and frozen organics that can persist over long geologic timescales and evolve under the influence of the Mercury space environment. Polar ices never see solar photons because at such high latitudes, sunlight cannot reach over the crater rims. The craters maintain a permanently cold environment for the ices to persist. However, the magnetosphere will supply a beam of ions and electrons that can reach the frozen volatiles and induce ice chemistry. Mercury's magnetic field contains magnetic *cusps*, areas of focused field lines containing trapped magnetospheric charged particles that will be funneled onto the Mercury surface at very high latitudes. This magnetic highway will act to direct energetic protons, ions and electrons directly onto the polar ices. The radiation processing of the ices could convert them into higher-order organics and dark refractory materials whose spectral characteristics are consistent with low-albedo materials observed by MESSENGER Laser Altimeter (MLA) and RADAR instruments. Galactic cosmic rays (GCR), scattered UV light and solar energetic particles (SEP) also supply energy for ice processing. Cometary impacts will deposit H_2O, CH_4, CO_2 and NH_3 raw materials onto Mercury's surface which will migrate to the poles and be converted to more complex C–H–N–O–S-containing molecules such as aldehydes, amines, alcohols, cyanates, ketones, hydroxides, carbon oxides and suboxides, organic acids and others. Based on lab experiments in the literature, possible specific compounds produced may be: H_2CO, HCOOH, CH_3OH, HCO, H_2CO_3, $CH_3C(O)CH_3$, C_2O, C_xO, C_3O_2, C_xO_y, CH_3CHO, $CH_3OCH_2CH_2OCH_3$, C_2H_6, C_xH_y, NO_2, HNO_2, HNO_3, NH_2OH, HNO, N_2H_2, N_3, HCN, Na_2O, NaOH, CH_3NH_2, SO, SO_2, SO_3, OCS, H_2S, CH_3SH, even B_xH_y. Three types of radiation processing mechanisms may be at work in the ices: (1) Impact/dissociation, (2) Ion implantation and (3) Nuclear recoil (hot atom chemistry). Magnetospheric energy sources dominate the radiation effects. Total energy fluxes of photons, SEPs and GCRs are all around two or more orders of magnitude *less* than the fluxes from magnetospheric energy sources (in the focused cusp particles). However, SEPs and GCRs cause chemical processing at greater depths than other particles leading to thicker organic layers. Processing of polar volatiles on Mercury would be somewhat different from that on the Moon because Mercury has a magnetic field while the Moon does not. The channeled flux of charged particles through these magnetospheric cusps is a chemical processing mechanism unique to Mercury as compared to other airless bodies.

1. Introduction

A surprising result from ground-based and spacecraft observations of Mercury is that water ice and other volatiles appear to be hiding in permanently-shadowed regions (PSRs) near Mercury's poles. The Sun's heat cannot reach into these shadowed areas

* Corresponding author.
E-mail address: cal_specialty@yahoo.com (M.L. Delitsky).

http://dx.doi.org/10.1016/j.icarus.2016.08.006
0019-1035/

because of Mercury's low obliquity. Polar ices never see direct sunlight because at such high latitudes, solar photons cannot reach over the crater rims. Only scattered light will reach them. The craters maintain a permanently cold environment for the ices to persist and so their temperatures can stay at < 100 K for many centuries. (Obliquity is currently at $\sim 0°$ from its orbital plane). Thermal model results show that in these polar craters, temperatures are cold enough to inhibit sublimation of water ice and other ices for longer than a billion years (Paige et al., 2013). Radar backscatter images from Earth-based observations show that Mercury's PSR's have unusually high radar backscatter cross sections suggesting the presence of thick, relatively pure water ice deposits (Slade et al., 1992; Black et al., 2010; Harmon, 2011; Cremonese et al., 2010; Solomon 2011). Indications of water ice are also seen in data from the MESSENGER neutron spectrometer (Lawrence et al., 2013). MESSENGER Laser Altimeter (MLA) and Dual Imaging System (MDIS) observations show that the surfaces of the Mercury's north polar PSR regions are uniformly covered by dark material of unknown composition in regions where subsurface water ice is thermally stable (Neumann et al., 2013; Chabot et al., 2012, 2014). These instruments have also observed bright surface material in the permanently shadowed region of Prokofiev crater where thermal models predict the presence of thermally stable surface water ice (Neumann et al., 2013; Paige et al., 2012, 2013; Chabot et al., 2012, 2014).

Observations suggest that the composition of the dark surface material in Mercury's PSR's is distinctly different from that of typical Mercury silicate regolith. MLA reflectance measurements at 1064 nm wavelength show that the normal albedo of this material is $\sim$ 0.04, which is half the normal albedo measured in adjacent non-PSR regions (Neumann et al., 2013). MDIS images illuminated by scattered sunlight obtained at visible wavelengths show that the coverage of the dark material within the PSR's is extremely uniform and that the boundaries of the dark deposits conform closely to those of the permanently-shadowed regions (Chabot, 2014). See Fig. 1. Thermal model results show that the bi-annual maximum surface temperatures of MLA-dark deposits in the north polar region are $\sim 175 \pm 50$ K (Paige et al., 2013). These temperatures are distinctly higher than the expected thermal stability temperature for exposed pure water ice of $\sim$100 K (Watson et al., 1963). Paige et al. (2013) hypothesized that the dark material covering Mercury's PSR's is rich in a low-albedo organic material. Similar material is observed covering the surfaces of comets as well as asteroids and primitive outer solar system bodies (Johnson, 1991a; Mumma and Charnley, 2011). Paige et al. (2013) calculated that the ice deposit would disappear on time scales of tens of thousands of years if not thermally protected by a $\sim$10-cm-thick layer of overlying ice-free material. They state that the volatile organic material delivered to Mercury via cometary or asteroidal impacts may become cold-trapped in the permanently-shadowed regions along with water ice and ultimately become exposed at the surface as a sublimation lag deposit. The spatially organized state of Mercury's polar deposits suggests that they are geologically young and are being actively maintained by ongoing processes in Mercury's PSR's. However, the actual composition of this dark material and their origin remains a mystery.

Darkening of the surface material at 1064 nm is not unambiguously a detection of organics. However, a covering of organic material provides a solution for the issue of water ice stability. Thermal models show that water ice will be unstable in many of the radar-observed ice-rich areas unless buried (Paige et al., 2013) implying that these deposits were buried on timescales faster than the time it would take for the ice to sublimate: about 1800 years kg^{-1} m^{-2} at 130 K, or 3.5 years per kg^{-1} m^{-2} at 150 K. If the original material creating both the bright and dark deposits arrived simultaneously (from comet origin), complex organics could quickly create a lag deposit of material burying the water ice below. This would occur from evaporation of the underlying water ice, leaving less volatile organic materials to accumulate. Radar absorption properties of low-density macromolecular organic carbonaceous materials are typically less lossy than low-density silicate soils expected in Mercury surface materials and so can be distinguished. Organic-rich materials overlying ground ice deposits, or organic macromolecular materials present in minor concentrations within ice deposits, are not inconsistent with the radar observations. (Paige et al., 2013). The dark material is more likely to be the product of chemical and radiation processing of icy volatile materials via energy deposition from the variety of sources available to Mercury's surface. This type of processing can yield crusty high-molecular weight organic materials that could act as a covering of the solid water ice below and thereby stabilize it against sublimation.

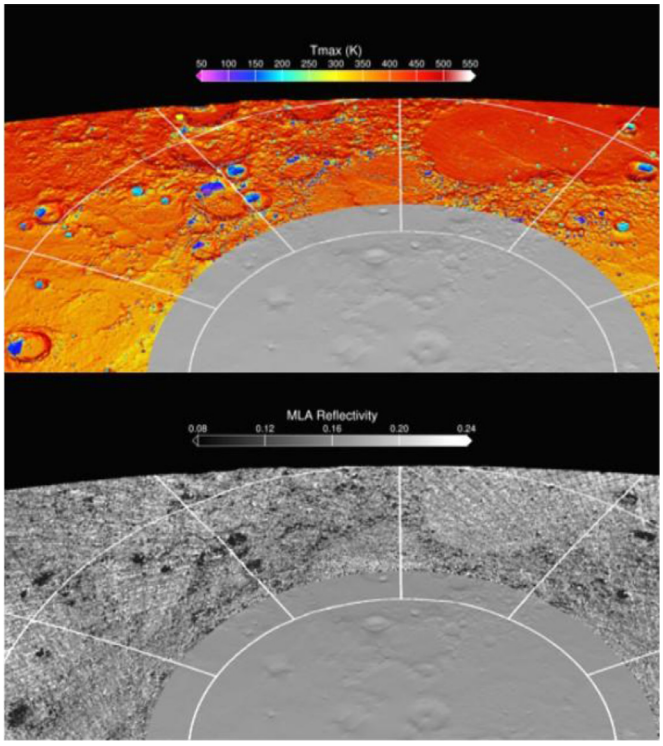

Fig. 1. (Upper) Calculated Bi-annual maximum temperature from Paige et al. (2013) for the North Polar region of Mercury. (Lower) MLA reflectance from same region showing "dark" material in areas remaining below $\sim$350 K, and "bright" material in areas remaining below $\sim$100 K. Data for the gray circle about the pole has not yet been published.

In this paper, we describe chemical and radiolysis processes that may be occurring in Mercury's polar regions where permanently frozen icy volatiles residing in cold traps are converted into dark refractory organics by energy input from many sources. Mercury's polar magnetospheric space environment sets it apart from that of other airless bodies in the solar system including the Moon and we propose that its unique properties may explain the present existence of abundant dark organics persisting in the polar regions on Mercury.

2. Magnetospheric particle precipitation near Mercury's poles

The first reconnaissance of Mercury was done by the Mariner 10 spacecraft during its 1974–1975 flybys. Its particles and fields measurements were the first indication that Mercury has a significant dipole magnetic field that is strong enough to deflect solar wind ions (Ness et al., 1974; Ness et al., 1975; Slavin, 2004). The MESSENGER spacecraft flyby and orbital data from its mission

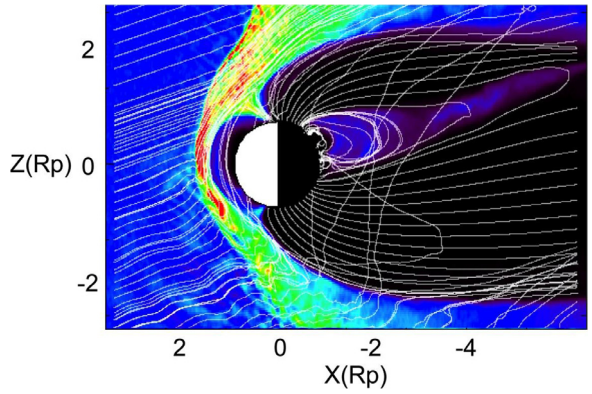

Fig. 2. Plasma density contours of Mercury's magnetosphere from MESSENGER observations. The Sun is to the left and the solar wind moves from left to right. The white traces show magnetic field lines. The cusps are the funnel shaped regions that come down to the planet at high latitudes in the northern and southern hemispheres.

operations in 2008–2015 has provided a more complete picture of the properties and dynamic nature of Mercury's magnetosphere as it is sculpted by the solar wind. Fig. 2 shows plasma density contours of Mercury's magnetosphere from a global hybrid simulation of the solar wind interaction with Mercury's intrinsic magnetic field. MESSENGER particles and fields instruments observed a wide array of energetic charged particles (protons, electrons and heavy ions) in various regions of the magnetosphere (Zurbuchen et al., 2008; Mouawad et al., 2011; McClintock et al., 2008; Ho et al., 2011; Schriver et al., 2011a, Schriver et al., 2011b; Raines et al., 2013, 2014).

The shapes of planetary magnetic fields are determined by the energies and contours of the solar wind (Russell, 2000). Planetary magnetospheres typically contain lobes on open field lines at very high latitudes on the polar caps, trapped plasma regions and plasma sheets on closed field lines in the equatorial region and funnels or "cusps" at the boundary between open and closed fields lines on the dayside at high latitudes. At Mercury, on the closed field line region, plasma (ions and electrons) from the plasma sheet precipitate at high latitudes ($\sim 45^o$–70^o latitude depending on solar wind conditions) forming an auroral-oval-type pattern in both the northern and southern hemisphere, whereas solar wind/magnetospheric ions and electrons precipitate at the cusp regions, which in the north can occur at polar latitudes $> 80^o$. The cusps create a high-flux stream of particle radiation focused onto Mercury's icy polar volatiles which could convert them to dark materials. Other sources of radiation energy delivered to the PSRs include solar energetic particles (SEP) from the Sun in the form of large solar flares and coronal mass ejections as well as scattered visible and UV photons and Galactic cosmic rays (GCRs).

One of the most important discoveries of the MESSENGER mission was that the location of the magnetic equator (the center of the dipole inside the planet) is offset by about 200 km to the north from the geographic equator (Anderson et al., 2011). That is, the center of the magnet in the interior is not at the core of Mercury but physically located 200 km north. This affects the shape of the charged particle precipitation onto Mercury's poles, particularly at the cusp. The magnetic moment of Mercury is large enough that it can stand off the plasma flux from the solar wind at most times, but at other times, the field lines will open and then the Mercury surface will be unprotected from charged particle fluxes. Since Mercury has no atmosphere or ionosphere, precipitation of charged particles directly impact the surface of the planet. This would cause sputtering and chemical reactions within surface materials. Molecules and atoms from sputtering are dissociated and photoionized, and then attached to field lines, where they become *recirculated* ions, moving up and down along the magnetic field. By this process, materials are transferred on this magnetic highway from the ice deposits and regolith to the exosphere and back again (Slavin, 2004; Chassifiere et al., 2010).

After two MESSENGER flybys of the planet (M1 and M2), Slavin et al. (2009) described the reconnection of the interplanetary magnetic field (IMF) to Mercury's magnetic field. Maps of precipitating protons from the solar wind onto Mercury's surface have been constructed using magnetohydrodynamic fluid simulations (Mouawad et al., 2011), hybrid simulations (Travnicek et al., 2010) and electron large scale kinetic simulations (Schriver et al., 2011a; Schriver et al., 2015; Domingue et al., 2014). Proton fluxes maximize at high latitudes, but there are also some equatorial hotspots. Proton flux intensities in excess of $10^8/(\mathrm{cm}^2\ \mathrm{s})$ occurred on these hot spots during the first MESSENGER flyby, M1 (Mouawad et al., 2011). The FIPS instrument observed three-dimensional plasma distributions detecting protons with energies around 1 keV flowing down into the northern cusp (Raines et al., 2013, 2014).

The location on the planetary surface where the cusps are focused is where the surface is unprotected. The cusp acts like a firehose, funneling ions and electrons onto the frozen materials in the polar regions. There are two cusps: one each near the north pole and south pole of Mercury. Due to ever changing solar wind conditions, the cusps move around over time depending on the orientation of the interplanetary magnetic field (IMF) (Slavin et al., 2014), which changes according to space "weather" emitted from the Sun (Baker et al., 2011). When the IMF has a northward tilt as depicted in Fig. 2, which occurred during the M1 flyby, the cusps are focused near the poles, $> 80^o$ latitude. When the IMF is southward directed, the cusp moves towards the equator (McClintock et al., 2009; Travnicek et al., 2010).

The cusps are mobile. They change location during *mass loading* events when the magnetic field lines can become swelled with solar wind plasma and then move southward toward the equator from the polar regions and become one big cusp (Slavin et al., 2010a, 2014). Slavin et al. (2010b) calculated that under normal conditions, 12% of Mercury's surface is open and unprotected from the solar wind and impinged by particles, but that during mass loading or *flux transfer events*, the cusps are bigger, so that 10–20% *more* (total $\sim$ 32%) of the surface could be open to the unimpeded radiation flux.

Here, we are interested in the precipitating fluxes when the cusps are furthest north, such that there is direct precipitation onto the north polar permanently shadowed ice deposits. Travnicek et al. (2010) simulated the interaction between the solar wind and Mercury's surface for the northward IMF to study the precipitating flux of solar wind *protons*. The precipitation profile can be seen in Fig. 3, where strong cusp precipitation is seen at 0^o longitude and polar latitudes $> 80^o$. Peak fluxes of $\sim 10^9$ $\mathrm{cm}^{-2}\mathrm{s}^{-1}$ occur at about 1 keV energy in general agreement with that found by Sarantos et al. (2009). The precipitation proton energy distribution follows a power law distribution with fluxes of $\sim 10^8$ $\mathrm{cm}^{-2}\mathrm{s}^{-1}$ at 10 keV energy.

Electrons also precipitate at the cusp regions. Large scale kinetic particle tracing simulations have been used to study the electron deposition onto Mercury for northern IMF conditions (Schriver et al., 2011a, 2015; Domingue et al., 2014). It was found that the strongest precipitation occurs at a very focused region at the high northern latitudes on the dayside. A 0.1–10 keV electron population precipitates to the Mercury surface at the cusps and in an auroral-oval-type pattern with fluxes of the order $\sim 10^9$–10^{10} cm^{-2} s^{-1}, depending on energy. Fig. 4 shows the average energy of precipitating electrons onto the northern hemisphere. The precipitating energy distribution approximately follows a power law, however, at the cusps there is a sharp energy cutoff with virtually no precipitating

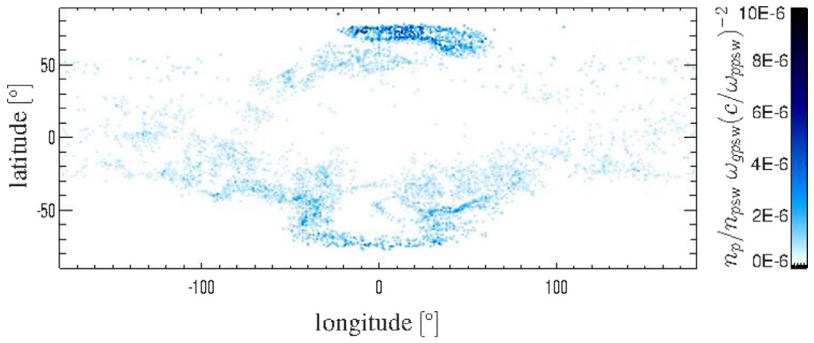

Fig. 3. A map of the simulated distribution of the proton flux precipitating onto Mercury's surface based on the model of Travnicek et al. (2010). The point (0, 0) corresponds to local noon. n_p is proton density, n_{psw} is proton density in the solar wind, c/ω_{ppsw} is proton inertial length in the solar wind. The darker blue region near noon at high latitudes (~ 0º longitude, ~ 80º latitude) is the location on the surface where the magnetospheric cusp comes down and the proton precipitation is greatest.

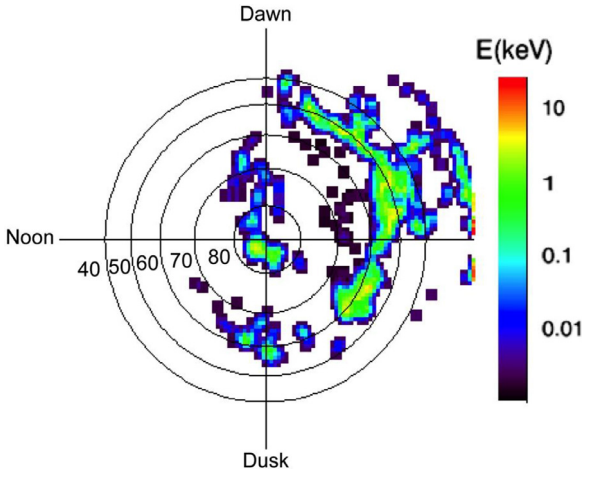

Fig. 4. Polar representation of the average energy E (in keV, color coded), of precipitating electrons onto the northern hemisphere of Mercury for the northward IMF solar wind configuration. The Sun is to the left and the geographic latitude of each circle is indicated. Note the enhanced energetic precipitation at latitudes > 80° N where the cusp is located. The precipitation at lower latitudes on the nightside corresponds to the auroral zone region with ions originating from the Mercury magnetosphere plasma sheet.

cusp particles with energies > 10 keV. At the cusps, peak fluxes of 10^{10} $cm^{-2}s^{-1}$ occur at 300 eV and fluxes of ~ 10^9 $cm^{-2}s^{-1}$ occur for 1 keV energies. Although there are occasional observations in Mercury's magnetosphere of very energetic electrons with energies > 30 keV (Dewey et al., 2015; Ho et al., 2016), these don't appear to be directed into the cusps, but rather at somewhat lower latitudes within the auroral oval precipitation pattern.

For the southern polar regions of Mercury, the flux of precipitating charge particles occurs over a larger area than in the north cusp, i.e. it has a bigger footprint (Winslow et al. (2012). The north cusp area is $\sim 5.2 \times 10^{15}$ cm^2 and the cusp area is $\sim 2 \times 10^{16}$ cm^2 in the south. The deposition rate of solar wind protons hitting the dayside southern cusp surface area is 1.3×10^{25}/s and for the dayside northern cusp, 2.5×10^{25}/s (Sarantos et al. (2009, 2011).

The south cusp lands at ~50°S, focusing the charged particles on mid-latitudes when the IMF is stable and the cusps are not moving. During M2, the charged particle impact rate at the northern cusp was four times higher than at the southern cusp (Benna et al., 2010). Frozen volatiles may also exist in the permanently shadowed craters in the south polar regions of Mercury, however the periapsis of MESSENGER in the south was much higher than in the north, so analysis of southern polar ices will have to wait for future observations.

Mercury's magnetosphere also contains many different heavy ion species, some also of multi-atom mass. Zurbuchen et al. (2008) observed these heavy ions during M1 using the Fast Imaging Plasma Spectrometer (FIPS) instrument. Closest approach was only 201 km above the surface. Na^+ dominates the heavy ions in Mercury's magnetosphere (Burger et al., 2010; Raines et al., 2013), but other ions detected include O^+, S^+, H_2S^+, O_2^+, H_2O^+ and C^+ (Zurbuchen et al., 2011). The carbon could have originated from the sputtering of frozen organics on the surface by the precipitating charged particles. Observations and modeling of sodium ions that precipitate directly into the cusps indicate that densities and fluxes are relatively low $< 10^6$ $cm^{-2}s^{-1}$ (Paral et al., 2010; Raines et al., 2013)

An important aspect of ion and electron precipitation is how deep these charge particles can penetrate into the regolith and/or water ice. The penetration range depends on charged particle type (ions, electrons) and energy. For water ice, ranges for electron traverse can be up to ~750 times the range of heavy ions. Protons and heavy atomic or molecular ions at solar wind energies reach down only to ~0.0001 cm. UV photons with wavelengths shorter than 2200 A are those that initiate chemistry (bond-breaking); these photons only reach down into the top tens of monolayers (~100–300A range). These ranges depend on density so they will be slightly longer for lower density organics or macromolecular materials in the lag deposits (Delitsky and Thompson, 1987). The deposition of particles creates a "cylinder of events" as they travel through the solid materials, causing ionization, dissociation, and free radical formation in excited states, depending on their energy and velocity (Chadderton and Torrens, 1969; Delitsky and Lane, 1998). These events occur at different depths, leading to stratified layers of new chemical species.

3. Other sources of radiation precipitation onto polar ices

The fluxes of galactic cosmic rays (GCR), UV photons and SEPs represent other sources of radiation precipitation in Mercury's polar environment. The population of GCRs consists of 85% protons, 12% alpha (helium nuclei), a small amount of heavy ions (C^{6+},O^{8+}, Si^{14+}, Fe^{26+}) and electrons (Johnson, 1990; Dartnell, 2011). GCR supply particles at a relatively constant lower flux than SEPs (Webber et al., 2007; Mishev 2013), but their spectra extend to very high energy levels (10^{20} eV); SEP energies range between 0.01–100 MeV with enhanced fluxes at the energies occurring sporadically as a function of active solar events.

Crites et al. (2013) studied the effect of galactic cosmic rays (GCR) on ices at the Moon's poles and found that, over the course of 1 billion years (Gyr), 6% of condensed volatiles could be converted to organic products. In their experiments on mixed H_2O, CO_2 and CH_4, ices, for every kilogram of ices, 60 g of ethane would be created over 1 Gyr. The depth of energy deposition depends on the density of the material (Crites et al., 2011). For the full

spectrum of proton energies, they report a depth of maximum energy deposition of ~33 cm. For ices below this maximum flux layer, the dose rate decreases with depth. GCR heavy ions, for example, iron (Fe^{+n}) are less abundant than protons but pack more "punch" as the loss of energy is proportional to the square of atomic number. Iron atoms deposit 24% of the total energy from the entire GCR particle spectrum. Maximum energy dose rate for a dry regolith of 0.1% water is given in Crites et al. (2013) as 1.24 MeV/cm^{3}s. For a wet regolith of 30% water, the energy deposition is 1.57 MeV/cm^{3}s because of the different cross sections for the materials. For the total GCR complement (protons, alpha particles and heavy ions), the maximum energy is 2.50–3.17 MeV/cm^{3}s for 0.1 and 30% water in the regolith, respectively.

Schwadron et al. (2012) estimated that GCRs deposited 88 eV/molecule in water ice or other volatiles over 4 billion years on the Moon creating complex molecules from carbon bonding with other elements in the ice. They calculate that the fraction of altered water ice is ~9% over a billion years from GCR deposition in lunar permanently shadowed craters. Tripathi et al. (2006) analyzed the lunar radiation flux for GCRs and solar proton events (SPE) such as coronal mass ejections (CME) and calculated that, for a CME event in 1989, the proton fluence was 1.39×10^9 protons/cm^2. For Mercury, the energy flux would be correspondingly higher ($r^2_{Earth}/r^2_{Mercury}$). Pilling et al. (2014) reported a flux on the Moon of 16 eV/molecule/Gyr and a proton fluence of 5×10^{17} electron/cm^2. They found that amino acids such as glycine will dissociate quickly under this fluence. Reitz et al. (2012) report a dose rate of 0.22–0.27 mGray/day on the lunar surface (1 Gray = 1 J/kg).

De Angelis et al. (2008) calculated effective dose and typical depth ranges of GCRs and SEPs in the Moon's regolith and bedrock (non-ice material, such as mare basalt). Their Fig. 8 shows dose for particles expressed in Sieverts/year. (Sievert (Sv), is a unit of radiation absorption which takes into account relative biological effectiveness of ionizing radiation). They report a total dose for all particles with a peak value of E = 0.3 Sieverts/year which occurs at ~0.8 m depth and then decreases, reaching zero at a depth of 6 m. GCR Protons peak at 0.24 Sieverts/year at the surface and go to zero by 6 m, while neutrons are greatest at 0.1 Sieverts/year at a depth of ~ 1 m, then drop off to zero by 6 m depth. From their computations of backscatter neutrons from interaction with the lunar surface, they report that SEP particles would be deposited to at least 80 cm depth, while GCRs could reach at least 2.5 m.

SEPs and GCRs should contribute to radiation processing of ices on Mercury over their entire range of deposition (centimeters to meters) and can account for the 10 cm depth of putative organic materials seen by MESSENGER radar.

For ultraviolet photon deposition, maximum deposition is at much shallower depths, a skin depth of nanometers. From ray-tracing thermal model results, the incident UV fluxes are calculated for the permanently shadowed craters. The model was originally used to calculate the temperatures in Mercury's north polar region (Paige et al., 2013) and includes the effects of multiply scattered solar and infrared radiation (Paige et al., 2010). The incident UV flux was calculated assuming that it includes the flux of solar photons with wavelengths of < 0.3 microns, which represents a small percentage of the bolometric solar flux for quiet Sun conditions. The scattered light UV flux is estimated to be ~1.0×10^9 eV/cm^{2}s for water ice regions, possibly higher for water ice buried under the dark organic lag deposits.

SEP events are enhanced fluxes of solar wind particles with energies ~100 keV and above (Mewaldt, et al., 2007; Desai et al., 2016). For such high energies combined with the relatively small magnetic dipole moment of Mercury, the magnetosphere has little effect on SEPs and their precipitation is approximately evenly distributed over the (primarily) dayside region of the planet. The magnetic focusing of the cusp that occurs at lower energies would not occur for SEP at high polar latitudes where the water ice and organic deposits are located and thus SEP fluxes into this region are comparatively lower. Nevertheless, there will be some precipitation near the poles as the SEP sweep over the planet. SEP events are usually associated with solar flares and coronal mass ejections (CME) or other large scale solar events (streamers, coronal holes, etc.), which occur sporadically with event rates of a few to several per year, which depends strongly on solar activity (Usoskin and Kovaltsov, 2012).

Using observations of SEP over an 8.25 year period (Fig. 3 from Mewaldt et al., 2007), we calculate the precipitating fluxes for protons (H^+) near the poles for different SEP energies using energy ranges 90–150 keV for the 100 keV value, 0.8–1.5 MeV for the 1 MeV value, 7–11 MeV for the 10 MeV value and 70–110 MeV for the 100 MeV value. The SEP proton fluxes range from ~10^3 particles/cm^{2}s at 100 keV to ~3 particles/cm ^{2} s at 100 MeV. The precipitating electron energy spectrum at lower energies (< 100 keV) follows a kappa (power law type) distribution function with peak energy at higher latitudes near 300 eV. Power law distributions have larger fluxes at higher energies compared to a standard Maxwellian. SEP precipitation will be an important contribution to the radiation processing of the ices and organics because of their comparatively greater depth of energy deposition compared with magnetosphere particles.

Table 1 summarizes the precipitating fluxes at different energies from all of the energy sources, i.e., Magnetospheric ion and electron cusp precipitation, SEP, GCR, Lyman-Alpha and scattered UV photons.

GCRs in the table are from Crites (2011, 2013); scattered light is from ray-tracing model results modified from LRO observations. Sources in E/cm^{2}s are, in some cases, derived by integrating dosage radiation (i.e. energy per cm^3/ time) over the depth of penetration. Photon energy deposition will be important at shallow depths (μm). GCRs and SEP will reach depths on the order of centimeters to meters.

As seen in Table 1, magnetospheric particle deposition is the dominant energy source onto the polar region with energy depositions ~10^{12} eV cm^{2}s. The total energy fluxes of photons, GCRs and SEP are each at least two or more orders of magnitude *less* than those from magnetospheric energy sources (the focused cusp particles). However, since depth depends on energy, each particle or photon will have their greatest energy deposition over a range of different depths in the ices (Delitsky and Lane (1998), Fig. 5).

4. Sources of volatiles and organics

The major sources of volatiles and organics at Mercury's poles are most likely from impacts of comets, asteroids and also possibly interplanetary dust particles, (IDP's) over the entire planet (Ishii, et al., 2008; Moses et al., 1999; Bruck Syal et al., 2013; Butler, 1997) and subsequent migration to the cold traps at high latitudes. Comets contain a frozen mixture of volatiles mixed with silicates and other stony or rock-like materials. Typical chemical composition includes H_2O, CH_4, NH_3, CO_2, CO, H_2S, H_2CO, C_2H_2, C_2H_6, CH_3OH, $HOCH_2CH_2OH$, HCOOH, C_3O_2 and others (Mumma and Charnley, 2011; Huntress and Delitsky, 1988; Huntress et al., 1991). Asteroids have water in the form of hydrated minerals as well as organics, mostly in the form of aromatic compounds such as PAHs, with additional aliphatic hydrocarbons and amino acids (Botta and Bada, 2002a, 2002b; Botta et al., 2002). IDP's contain both organic and inorganic ices (Ishii, 2008). Retention of volatiles on the Moon from cometary impacts was estimated to be ~0.1% of a cometary mass, but could yield a ~1 mm thick water ice layer in the cold traps from each impact. Large amounts of water ice consistent

Table 1
Compilation of precipitating energy fluxes from all sources onto Mercury's north polar regions.

Particle	Energy	Flux (cm^{-2} s^{-1})	Deposition rate eV cm^{-2} s^{-1}
Magnetospheric electrons (Schriver et al., 2015)	300 eV	1.1×10^{10}	3.3×10^{12}
	1 keV	4.2×10^{9}	4.2×10^{12}
	10 keV	3.8×10^{8}	3.8×10^{12}
Magnetospheric Protons (Travnicek et al., 2010)	1 keV	4.3×10^{9}	4.3×10^{12}
	10 keV	2.5×10^{8}	2.5×10^{12}
SEP Protons (Mewaldt et al., 2007)	100 keV	2.7×10^{3}	2.7×10^{8}
	1 MeV	7.3×10^{2}	7.3×10^{8}
	10 MeV	2.4×10^{2}	2.4×10^{9}
	100 MeV	3.4×10^{0}	3.4×10^{8}
GCR Protons (Crites et al., 2013)	1 GeV	3.0×10^{0}	3.0×10^{9}
Lyman Alpha (Pryor et al., 2013)	10.19 eV	1.0×10^{9}	1.02×10^{10}
Scattered UV Photons (our work)	$\lambda < 0.3$ μm		1.0×10^{9}

with spacecraft observations could accumulate over billions of years (Stewart et al., 2011). The relative importance of comets vs. asteroids vs. IDP's as volatile sources for Mercury is highly uncertain (Moses et al., 1999). Estimates from impacts during the late heavy bombardment could be useful for calculating volatile inventories.

5. Processing of organics

While comets appear to be very bright when they are traveling through the inner solar system, reconnaissance by spacecraft of comets such as Halley, Borrelly, Tempel 1, Hartley 2 and others have shown that most often they have extremely dark surfaces. The Vega spacecraft measured the albedo of Comet Halley to be 0.04 (+0.02, –0.01) (Sagdeev et al., 1986). Many laboratory experiments have shown that bright icy materials are transformed by charged particle radiation into an outer crust made up of polymerized long-chain hydrocarbons, tars or kerogens with many unsaturated bonds and high carbon/hydrogen ratios (Johnson et al., 1987; Lanzerotti et al., 1987a; Strazzulla, 1997; Strazzulla et al., 1984a). Heating of comets during their passage around the Sun will also darken the surface. Complex organic material was observed on Comet Halley from observations by the PICCA Mass Spectrometer onboard Giotto; mass fragments of > 50 amu were attributed to organic molecules (Mitchell et al., 1992).

When methane is bombarded with radiation, C–H bonds are excited and/or broken and the hydrogen atoms combine with each other to form H_2. Subsequent energy deposition causes more C–C bonding and cross-linking to form higher-molecular weight compounds (Johnson, 1991a, 1991b; Strazzulla et al., 1991). The products may be a disordered form of carbon, such as *ion produced hydrogenated amorphous carbon*, or IPHAC (Ferini et al., 2004; Strazzulla and Baratta, 1992; Strazzulla, 1997), or other polymeric products such as $C_{20}H_{40}$, $C_{25}H_{50}$, $C_{23}H_{46}$ as reported in Davis et al. (1966). IPHAC will have both aromatic and aliphatic ligands and no definable crystalline nature, due to the breakdown of crystal structure from the radiation. Aromatic compounds such as PAHs may also be formed, like those seen in asteroid carbon materials (Botta and Bada, 2002a, 2002b). Lightweight gaseous H_2 will escape the lattice leaving heavier atoms to form a "crust" or cometary "mantle" (Frank, 1986; Brown et al., 1987; Cheng and Lanzerotti, 1978). As a result, the total C/H ratio increases over time. C/H ratio depends on the amount of deposited energy. The density of this crusty refractory material increases with increased fluence of radiation (Strazzulla and Johnson, 1991; Strazzulla et al., 1984b; Lanzerotti et al., 1987b; Foti et al., 1984; Strazzulla et al., 1988). If enough H_2 escapes, ultimate products could include elemental carbon in some form (graphite, amorphous carbon, soot, carbon black) which will be very dark. An illustration of darkening of cometary ices by radiation is shown in Jewitt (2012).

Charged particles are slowed in their paths as they traverse deeper into surface layers of the condensed volatiles and the energy deposition will have a maximum at some depth as the particles slow down and then stop in the material. The depth at which the greatest amount of energy is deposited is called the *Bragg peak* (Strazzulla et al., 2003). The thickness of the crust created depends on the penetration depth, *not* on dose. The location of the maximum rate of energy loss, i.e., the depth of the Bragg peak, is near the end of the maximum penetration depth for an incident particle of particular energy and mass. The depth profile of dosage rate is computed from the superposition of a large number of individual energy deposition profiles from separately incident particles, mainly from superposition of the Bragg Peaks, and related to the incident particle flux. The thickness of the dark crust is determined by the maximum penetration depths of particles with significant incident flux.

In experiments by Lanzerotti et al. (1987b) and Strazzulla and Johnson (1991), frozen methane under proton bombardment converted from a bright ice to an increasingly darker material. The end product was a highly carbonaceous material (90%) that is black. The density increased from 0.5 g/cm^3 for frozen methane to 0.75 g/cm^3 for the black carbonized refractory material. Johnson (1991a, 1991b) reported a decrease in H/C ratio from 4 to ~1.5–2 over the irradiation time when CH_4 was irradiated by MeV protons and helium ions (used as a proxy for galactic cosmic rays or solar wind). That is, $CH_4 \rightarrow CH_{1.5-2}$ over irradiation time.

Physical effects on the ices from deposition of energetic particles include the creation of voids, dislocation of atoms, amorphization of the crystalline ice lattice and defects that can form connecting paths through the material (Chadderton and Torrens, 1969; Lanzerotti et al., 1987b; Domingue, 2014). These paths may eventually be open to the vacuum of space. The material becomes increasingly porous even as it increases in density. Radiation causes breakdown of crystals into amorphous materials (Johnson, 1991a, 1991b; Stern, 2003).

CO_2 and CO ice in comets can be polymerized by incident radiation into mixed C_xO_y species, such as carbon suboxide C_3O_2 (Geiger, 2013; Geiger and Staack, 2011, 2012) and analogs C_5O_2 and other C_nO_2, as well as C_2O, C_3O, C_4O, C_5O, C_6O, C_7O and their polymers (Strazzulla et al., 2011; Bennett et al., 2008; Jamieson et al., 2006). These materials may have color and be dark or black as well (Fridman et al., 2006). C_3O_2 can be either red, brown, violet or yellow, depending on temperature; it converts to elemental carbon at temperatures > 500 C.

Nitrogen occurs in comets, either as molecular nitrogen, N_2, or ammonia NH_3.(Wyckoff et al., 1991; Biver et al., 2012; Rubin et al., 2015). N atoms can be incorporated into growing hydrocarbon

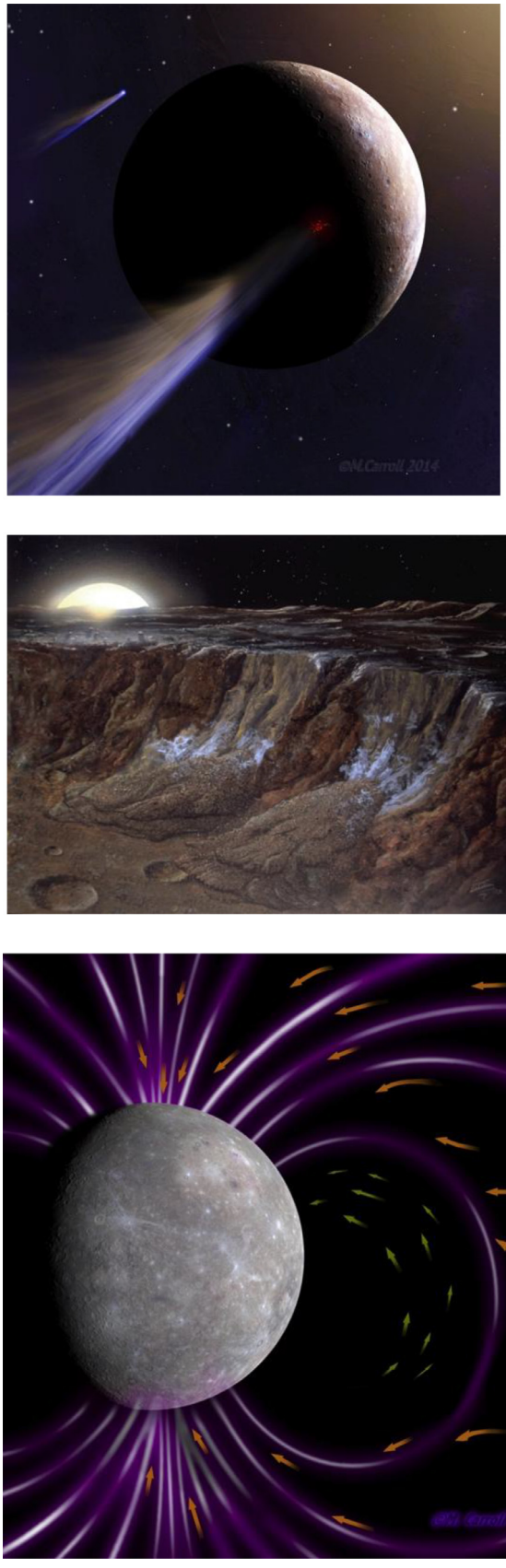

Fig. 5. Polar ices on Mercury. Panel 1: Delivery of icy volatiles from comets Panel 2: Ice hiding in permanently shadowed craters Panel 3: Trapped magnetosphere ions follow field lines to Mercury's poles and impact ices. (Artwork by Michael Carroll).

polymers to yield C-N/HCN polymers (Matthews and Ludicky, 1986). These are often black-brown solids (Ruiz-Bermejo et al., 2009). This type of polymer is thought to be a component of the dark crust of Comet Halley (Matthews and Ludicky, 1986).

Mercury's polar ices are estimated to be meters thick. From the calculation of sublimation rate for organic compounds over a range of temperatures, Zhang and Paige (2009, 2010) showed that a variety of large and small organic molecules may be cold trapped. The sudden heating of comets by impact will convert smaller molecules into heavier, less volatile molecular species. However, heavier-weight species inside the comet may survive the impact of the comet intact (Blank et al., 2001). The effect depends on the pressure-temperature history of the comet during impact, its density ("fluffiness"), and also on the *angle* that it hits Mercury (Blank, 2009; Ross, 2006). Low angles favor preservation of organics (Liu, 2007). Fig. 5 shows the sequence of the supply of materials to the Mercury surface: cometary volatile delivery by impact (top panel), ice hiding inside shadowed craters (middle panel), and cusp radiation as the energy source (bottom panel). With enough processing, dark polymers may eventually be converted into elemental carbon. Then the polar craters will be covered with soot which will be very dark indeed.

6. Organic yields

To calculate product yields for organics, the G value (radiation chemical yield) is used. G is the number of product molecules produced for every 100 eV of energy deposited. Various authors have reported G values for methane radiolysis that vary between 0.1–2.0, depending on the product (Davis et al., 1966; Scott and Wilson, 1968). Mozumber (1999) reported a G value = 2 for conversion of methane to liquid polymer. Davis et al. (1966) calculated G values for processing of methane into other hydrocarbons, including polymers such as $C_{20}H_{40}$, $C_{25}H_{50}$, $C_{23}H_{46}$ and others. For production of the total products, Davis gives G = 0.32/100 eV. Meisels et al. (1957) reported G values (from methane) for ethane, propane, butane and hydrogen as $G(C_2H_6)$=0.7, $G(C_3H_8)$=0.1, $G(C_4H_{10})$=0.05, $G(H_2)$= 2.0.

For the purposes of illustrating organic yields, as an example, we use the conversion of methane ice into heavier weight products (G value = 0.32 from Davis et al. 1966) hereto referred to as "Polymer":

The column density of products, C, is calculated from:

$$C = E\,F\,G\,t,$$

where

E = energy (in eV/particle),
F = charged particle flux (in cm^{-2} s^{-1}),
G = yield of product molecules/100 eV deposited
t = time of irradiation.
AS AN EXAMPLE:
For protons, if:
$E_{protons}$ = ~1 keV
F = 10^9 protons/cm^2 s
G = 0.32 molec/100 eV
then for every square centimeter,
Production rate of Polymer=
1000 eV/particle * 10^9/cm^2 s * 0.32 molecules Polymer/100 eV
= 3.2×10^9 molecules Polymer /cm^2 s.
Over the age of the solar system, 4.5 billion years,
Column density of Polymer from proton deposition is:
1.42×10^{17} s * 3.2×10^9 molecules Polymer /cm^2 s
= 4.54×10^{26} molecules Polymer /cm^2

(This assumes that the entire energy of the particle (1 keV) gets deposited in the ice and is used for chemical processing. Average

energy of protons is 1 keV but there is a higher energy tail on the distribution that will increase the production rate from these values. The same holds true for electron energies; amounts of products and depth of deposition will be larger.)

For *electrons*, if:
Average electron energy = 300 eV.
Electron flux = 10^{10} /cm^2 s,
Production rate of Polymer =
300 eV/particle * 10^{10} particles/cm^{2}s * 0.32 molecules Polymer/100 eV
= 9.60×10^9 Polymer molecules/cm^2 s.

For electrons, the column density of Polymer is:

1.42×10^{17} s * 9.6×10^9 Polymer molecules/cm^2 s
= 1.36×10^{27} Polymer molecules/cm^2.

Total Polymer: $4.54 \times 10^{26} + 1.36 \times 10^{27} = 1.81 \times 10^{27}$ molecules Polymer /cm^2.

For an estimate of the thickness, T, of an organic layer generated in a year on Mercury (using naphthalene as an example product from methane bombardment by electrons):

$T = C^*V$

$C = P^*S$

$V = (1/\rho)^*(m/A)$

where:

1. ρ = density of product molecule = 1.14 g/cm^3
2. m= molecular weight = 128.17 g/mole
3. A= Avogadro's number = 6.02×10^{23} molecules/mole
4. m/A = mass of a molecule = 2.13×10^{-22} g/molecule
6. V = volume of molecule = 2.13×10^{-22} g/molecule / 1.14 g/cm^3 = 1.86×10^{-22} cm^3/molecule
7. P = Production rate = 9.6×10^9 molecules/cm^2 s
8. S = Seconds/year = 3.153×10^7
9. C = Column density = Rate × Seconds = 3.02×10^{17} molecules/cm^2
10. C × volume = Column density/time = C × volume (1.86×10^{-22} cm^3/molecule) = 5.6×10^{-5} cm /year
11. T = Thickness generated = ~ 0.56 um /year

Therefore, around 0.56 micrometer of dark material will be formed per year from irradiation of ices residing in polar craters.

Electron energies were measured at between 0.3–10 keV (Schriver, 2015; Starr et al., 2012); if the top energy of 10 keV was used, we would derive a production rate 33 times higher, or 3.16×10^{11} Polymer molecules/cm^2 s, yielding ~18.6 micrometers of material per year.

In the above example, we've assumed a target of pure methane ice for illustrative purposes. Pure methane ice is too volatile to be cold trapped at Mercury's poles, but a range of higher molecular weight compounds with similar hydrocarbon structure will have the correct volatilities to be cold trapped (Zhang and Paige, 2009; Paige et al., 2013), and would be expected to undergo similar transformation.

A few caveats in the above discussion are that yields of heavier weight compounds from methane could be upper limits because the formation of a crust of organics might tend to reduce the amount of other products formed. The incoming ions arriving later find an already formed crust and cannot produce further layers. However, gardening rates for ices and creation of new regolith is estimated to be ~ 10^{-9}–10^{-10} m/year (Jewitt et al., 2007), so organic formation from radiation processing could be happening fast compared to gardening, if Jewitt's estimate is correct. However, a 1 nm/year gardening rate may be appropriate to lunar regolith with no ice, but impacts of silicate 10–100 micron particles on water ice have yields less than or equal to ~ 10^5 of ejected mass per unit incident mass as calculated for water ice on Saturn's rings (Cuzzi and Estrada, 1998). Ignoring other differences between Saturn's rings and the Mercury polar ices, the gardening rate could be about 1 micron/year. Mercury would also experience impacts from the solar dust cloud, as well as from interstellar dust as at Saturn.

The actual depth of particle deposition will vary with energy and type of charged particle (Paranicas et al. 2009). Particles such as GCRs and SEPs at > 1 keV will irradiate much deeper layers than magnetospheric ions. The particles and their chemical products would form distinct layers. Mejia et al. (2013) reported that solar wind ions will implant in the top 1 micron depth in ices; whereas they found GCRs in layers at between 1 and 100 mm depth. Using the "continuous slowing down approximation" (CSDA) for particles traversing solid materials, the approximate ranges, r, for electrons and protons in hydrocarbon material are:

Electrons: Energy, Range

300 eV, 0.02 micron.
1 keV, 0.06 micron.

Protons: Energy, Range

1-keV, 0.04 micron.
1.0 MeV, 20 micron.
10 MeV, 1 mm.
100 MeV, 10 cm.

Below, we consider in greater detail the chemical transformation mechanisms that should be operating in Mercury's polar volatiles.

7. Chemical effects of charged particle deposition on ices

Chemical effects from charged particle irradiation on solid icy materials can cause three types of chemical reactions:

(1) *dissociation of molecules by impact of magnetospheric ions and electrons* to form new products (Hudson and Moore, 1995; Moore and Khanna, 1991),
(2) *implantation of magnetospheric ions into ices* and their participation in subsequent chemistry (Dawes et al., 2007; Hunniford et al., 2009; Roessler, 1985a, 1986, 1992; Roessler et al., 1985; Roessler and Eich, 1988);
(3) *"nuclear recoil" reactions* (or *"hot atom chemistry"*) where impact from GCR and SEP particle deposition onto surface materials converts an atom of one isotope of an element into an isotope of a different element (Roessler, 1986,1988).

1. In the first process, that of dissociation of molecules by impact of heavy ions or electrons, the impactor may not be participating in the reactions and only act as a "battering ram" to break the bonds and form new products (Strazzulla et al., 2003, 2011). The impactor may also induce *amorphization* of a crystalline material: breaking down the lattice structure into amorphous particles that have lost any symmetry or crystalline nature (Loeffler and Baragiola, 2009). Hudson and Moore (1999) irradiated CO/H_2O ices with protons and obtained HCOOH, CH_3OH, HCO and H_2CO. Irradiation of CO_2/H_2O ices yields H_2CO_3 (carbonic acid) (Gerakines et al., 2000, Peeters et al., 2010; Moore et al., 1991) as well as HCOOH (formic acid), $CH_3C(O)CH_3$ (acetone), CH_3OH (methanol) and others. (See CO_2/H_2O chemical pathways in Delitsky and Lane, 1997;1998). Irradiation of CO ice with energetic electrons yields *cumulene* structures, C_xO_y (Jamieson et al., 2006) where carbon atoms are attached to each other with consecutive double bonds with oxygen atoms at each end, such as O=C=C=C=O. Molecules

that have consecutive double and triple bonds have delocalized electrons which causes their spectral absorption bands to move from the ultraviolet into the visible and so the materials may have color (Benit et al., 1988).

2. In the second process, an impacting ion implants itself into condensed volatiles. Products are created that include the implanted ion (Strazzulla, 2011; Dawes et al., 2007; Hunniford et al., 2009; Delitsky and Lane, 2002). Implantation of carbon *ions* (C^+) as well as carbon *atoms* (C) into water ice yields CO_2 (carbon dioxide), HCOOH (formic acid), $CH_3C(O)CH_3$ (acetone), CH_3CHO (acetaldehyde) and $CH_3OCH_2CH_2OCH_3$ (1,2-dimethoxyethane) (Roessler and Eich, 1988; Lv et al., 2012). Zurbuchen et al. (2008) detected carbon ions, C^+ in the Mercury magnetosphere; if these ions impact and deposit into water ice, then oxidized carbon-containing products such as these may be created.

Roessler (1986) reported a variety of products resulting from carbon ion deposition into water ice:

$$C^+ + H_2O \rightarrow CO_2 + H_2CO + CH_3OH + HCOOH + CO + CH_4 + CH_3C(O)CH_3 + CH_3CHO + CH_3OCH_2CH_2OCH_3.$$

If C^+ implants into *mixed* cometary ices, such as H_2O, NH_3 and CH_4, products may be *amino acids, amides, purines, pyrimidines*, and other C-N-O-H-containing molecules (Roessler, 1985a, 1985b, 1986). Impact of electrons, protons, or C^+ ions into NH_3 ice could produce hydrazine (N_2H_2), azides (N_3), hydrogen cyanide (HCN) and CH_3NH_2 (Roessler and Eich, 1988; Roessler and Nebeling, 1987, 1988). CH_3OH may form precursors to *biomolecules*: formaldehyde converted into sugars, cyanamides into polypeptides or guanidine into nucleic acids (Roessler, 1986).

In the reaction of $C^+ + H_2O$, carbon inserts into the O-H bond in water to make HCOH and this rearranges to make formaldehyde H_2CO and other $C_xH_yO_z$ (Baratta et al., 2012; Strazzulla, 2011; Roessler, 1986). The deposition of sulfur ions (as S^+ detected in Mercury's magnetosphere) into water ice may yield SO, SO_2, and SO_3 (Boduch et al., 2015; Sack et al., 1992; Delitsky and Lane, 1997, 1998) as observed on the Jovian satellites (Lane et al., 1981). Deposition of Na^+ into water ice may yield Na_2O and NaOH (Brown and Hill, 1996; Delitsky and Lane, 1997).

3. The third process causing chemical change is "nuclear recoil", also called "hot atom chemistry". Fast impact of high-energy charged particles will cause nuclei to undergo isotope transformation, which would convert them into other elements. Roessler (1986, 1988) found that an oxygen atom, ^{16}O deposited into water ice and then bombarded with protons via a cyclotron will convert it into a nitrogen isotope, ^{13}N. Subatomic particles from the oxygen nucleus are released (knocked off in a fission process). The oxygen atom has now become a nitrogen atom which then acts accordingly. Its chemistry is that of nitrogen rather than oxygen. The new ^{13}N is called a "recoil nuclei". It now finds itself inside water ice and it is kinetically hot as though it had implanted at high velocity itself. New products created were: ^{13}NO (nitric oxide), $^{13}NO_2$ (nitrogen dioxide), $H^{13}NO_2$ (nitrous acid), $H^{13}NO_3$ (nitric acid), $^{13}NH_3$ (ammonia), $^{13}NH_2OH$ (hydroxylamine), $H^{13}NO$ and polymers. In other experiments, Roessler deposited ^{14}N isotopes into water ice, bombarded the sample with cyclotron particles, and created ^{11}C. Nitrogen atoms had become carbon atoms inside the water ice and reacted to create products ^{11}CO, $^{11}CO_2$, $H^{11}CO$, $H_2{}^{11}CO$, $^{11}CH_3OH$, $H^{11}COOH$ and others. The newly created and kinetically excited carbon atom arising from the recoil reaction then becomes a participant in the chemistry as carbon (Roessler, 1985b; Roessler and Nebeling, 1987, 1988). See Fig. 6.

The keV-MeV energies of magnetospheric particles are insufficient to induce nuclear recoil reactions and conversion to other elements. Magnetospheric charged particles are only energetic enough to cause ionization of atoms and dissociation of molecules in the ices, creating free radicals, possibly in the excited state. GCRs have larger energies (GeV) and their impact could initiate transformation of atoms into other isotopes and then conversion into other elements by release of nuclides, as described above. Nuclear processes such as *spallation* may occur, in which a single nucleon, or a few nucleons (e.g., an alpha particle), are knocked out to form new isotopes, or *fragmentation*, in which an overly excited nucleus breaks up into fragments. There are also natural radioactive decays of nuclei which release particles that affect surrounding materials and do not require any impact by GCRs.

If a speeding GCR particle impacts a normal ^{14}N residing in a condensed volatile in Mercury's craters, it could convert it into a ^{11}C. However, this isotope of carbon has a half life of ~20 minutes, after which it decays to boron. Then the chemistry becomes that of boron; so this process (N → C → B) would possibly yield boron compounds such as B_xH_y, boron hydrides or "boranes", resulting from reaction of boron with water ice.

By this recoil process, oxygen atoms in H_2O ice on Mercury could be converted into N atoms which are still bonded to hydrogen atoms, thereby making ammonia, NH_3, in-situ. Nuclear recoil reactions also occur in liquids and gases (Roessler, 1985b). If a sulfur atom is created from the splitting of heavier isotopes, then reacts with H_2O, CH_4 or CO_2, products may be organic sulfur compounds such as H_2S, CH_3SH, or sulfur polymers. These are dark materials. Reactions of sulfur atoms with CO_2 ice will yield OCS.

8. Physical effects of charged particle deposition on ices

At the time that chemical effects are occurring in the ices, physical effects are happening simultaneously which will also affect their size, texture, density, temperature and chemistry. Domingue (2014) described many of these processes:

(1) *sputtering*
(2) *solar wind deposition*
(3) *photo-stimulated desorption*
(4) *meteoroid bombardment and volatilization*
(5) *radiogenic heating from the regolith*
(6) *thermal desorption*
(7) *electron-stimulated desorption*
(8) *dust levitation*
(9) *surface charging*
(10) *impact gardening*
(11) *secondary sputtering from recirculated planetary ions in the magnetosphere*

These processes will create holes and dislocation of atoms in ices or regolith and change the density of the materials (Domingue et al., 2007; Hurley et al., 2012; Johnson et al., 2004). Charge deposition can cause dust grains to levitate above the surface. Sputtering of heavy atoms off of the surface populates the exosphere (Domingue et al., 2007, 2014). This "space weathering" or gardening will transform the ices and regolith into porous materials which may not be able to retain gases such as hydrogen as easily, thus releasing it and promoting cross-linking of C–C bonds and polymerization. Sputtering yield of water depends on temperature and electronic stopping power; this was measured by Dartois et al. (2015) to be between 2610–9100 H_2O molecules/impacting ion for water ice between temperatures 13.6–125 K. However, organic materials and water ice in the Mercury polar craters are likely to have long lifetimes against sputtering loss. Sputtering yields are very low for materials below 100 K but increase sharply above this temperature (Johnson et al., 2012). For the PSRs, the very cold temperatures below 100 K will limit sputtering loss to very low values.

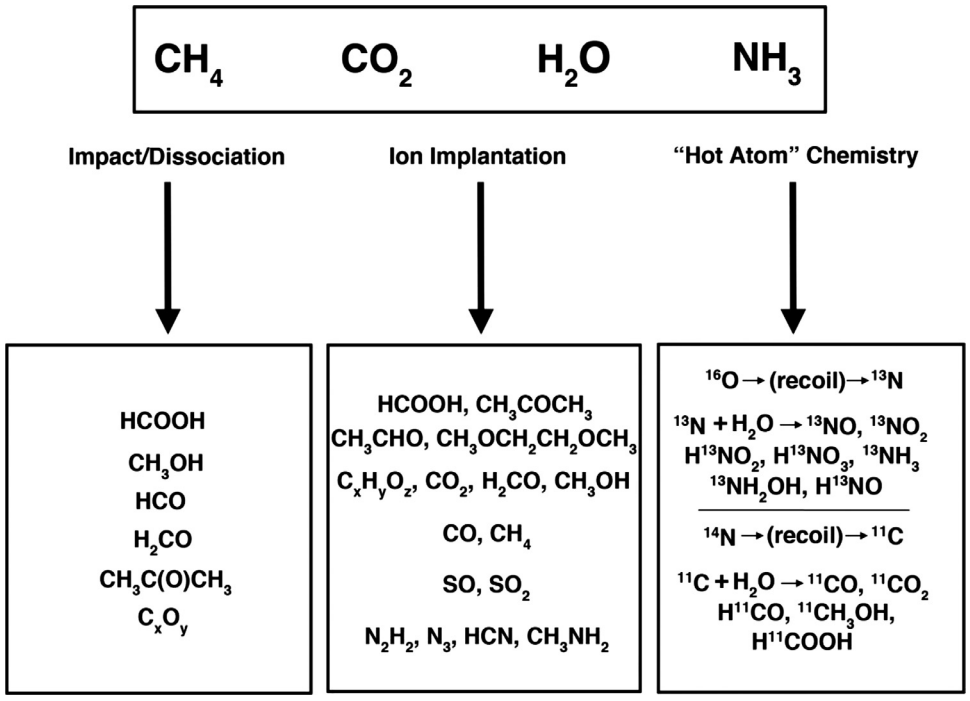

Fig. 6. Flowchart showing three types of reactions resulting from ion impact into ices: simple dissociation, implantation and hot atom chemistry.

9. Comparison between Mercury and the Moon

Water ice has been detected in the Moon's polar regions (Feldmann et al., 2001; Colaprete et al., 2010; Hayne et al., 2015; Paige et al., 2010; Nozette et al., 2001; Spudis et al., 2013; Anand et al., 2014; Crawford, 2015), but in far lower abundance than observed on Mercury. UV-dark surface material has been detected in the Moon's permanently-shadowed regions (Gladstone et al., 2012), but no visible-dark material like that found on Mercury. Why are the Moon and Mercury so different?

Possible explanations for the higher concentrations of cold-trapped volatiles at Mercury are: (1) the higher obliquity of the Moon in ancient times which resulted in less shadowed regions in the early history of the Moon (Siegler et al., 2011, 2013), (2) the lower gravity of the Moon which leads to less retention of volatiles compared to Mercury (Stewart et al., 2011), and, (3) the fact that the Moon orbits the Earth through the tail of its magnetosphere (Moses et al., 1999). This final hypothesis is plausible due to the increased sputtering by energetic particles over all latitudes on the Moon's surface, causing a greater loss of volatiles there (Jordan et al., 2013). Volatiles may not have time to migrate to the lunar poles because radiation at low latitudes may process them before they get a chance to sublimate and migrate (Hendrix et al., 2012). However, during times when the Moon passes through the Earth's magnetotail, total 1-keV proton fluxes were observed to decline by the twin lunar-orbiting ARTEMIS spacecraft, because of the magnetospheric deflection of solar wind protons, so there may not be higher sputtering fluxes at all lunar latitudes.

Whatever the explanation for the difference in cold trapped volatile concentrations between the two worlds, our work suggests one additional difference: the Moon does not have an intrinsic magnetic field or magnetosphere, so there are no cusps present which focus solar wind protons, electrons and heavy ions onto high latitudes as on Mercury. The main source of lunar protons is the solar wind, which impinges on the Moon at low angles relative to the moon's equatorial plane. At high latitudes, interiors of lunar craters may be shaded from direct solar wind protons in much the same way as they are shaded from direct solar photons (Lucey et al., 2014). Because of the focusing of precipitated protons by Mercury's magnetic field, Mercury's polar regions are preferred locations for charged particle bombardment.

While the GCR, SEP, Lyman Alpha and Scattered UV energy sources are similar on the Moon and Mercury, the magnetospheric proton energy sources are 100–1000 times greater on Mercury (See Table 1). As we have described, this focused "firehose" of particles can provide abundant energy that can drive chemical reactions which can polymerize cold-trapped volatile organics to produce dark, refractory lag deposits analogous to those found on the surfaces of comets and other primitive bodies. The additional energy sources also contribute to this chemical processing. The visible dark material on Mercury is associated with thick, radar-bright ice deposits, which are absent on the Moon. As suggested by Paige et al., 2010, the dark material may be a lag deposit that accumulates as water ice underneath sublimates, similar to the processes that create dark crusts on comets (Jewitt et al., 2012).

10. Conclusions

1. Mercury has funnel-shaped features in its magnetic field lines called *magnetospheric cusps*. These cusps touch the planet at high latitudes and will cause focusing of the flow of magnetospheric charged particles that are trapped on the field lines. The particle flow is directly aimed at Mercury's polar regions and their permanently-cold, permanently-shadowed craters. The ions hit at high enough angles to impinge directly onto cold-trapped ice deposits within these craters.
2. A variety of charged particle radiation sources and solar photons will initiate chemistry in the polar ices. The combination of Magnetospheric particles, Galactic cosmic rays (GCR), solar energetic particles (SEP), Lyman Alpha and scattered UV will deposit energy into the frozen volatiles and cause chemical reactions yielding new heavier-weight organic products. The magnetospheric particle energy depo-

sition is two or more orders of magnitude greater than each of the other energy sources.

3. Because Mercury has a magnetosphere, it has a unique space environment that influences the polar volatiles which is different from that on the Moon. The channeled flux of charged particles through these magnetospheric cusps is a chemical processing mechanism unique to Mercury as compared to other airless bodies.
4. The deposition of magnetospheric charged particles such as O^+, S^+, H_2S^+, O_2^+, H_2O^+, C^+, Na^+, H^+ into the ice should produce a variety of new C-H-O-N-S-containing compounds. The end products could include carbon-rich, polymeric, tar-like, refractory dark materials whose characteristics are similar to dark compounds observed in the polar craters by MESSENGER spacecraft instruments.
5. Three kinds of radiation processes that could initiate chemistry could be occurring in these ices:, (1) dissociation, (2) implantation of charged particles, and (3) nuclear interactions (creation of new isotopes and elements). Conversion into new isotopes and elements can be caused only by the higher energy GCR and SEP particles. Magnetospheric particles will induce ionization and dissociation.
6. Cometary impacts are the source of volatiles, depositing H_2O, CH_4, NH_3, CO_2, CO, H_2S and other raw materials onto Mercury which would eventually migrate to the polar regions. Classes of molecules formed from radiation processing of these raw materials could include hydrocarbons, ketones, esters, carboxylic acids, alcohols, amines, amides, purines, pyrimidines, sulfides, and cyanamides. From lab experiments in the literature, possible specific products are: H_2CO, HCOOH, CH_3OH, HCO, H_2CO_3, $CH_3C(O)CH_3$, C_2O, C_xO, C_3O_2, C_xO_y, CH_3CHO, $CH_3OCH_2CH_2OCH_3$, C_2H_6, C_xH_y, NO_2, HNO_2, Na_2O, NaOH, HNO_3, NH_2OH, HNO, N_2H_2, N_3, HCN, CH_3NH_2, SO, SO_2, SO_3, OCS, H_2S, CH_3SH, even B_xH_y.
7. The impact of many energy sources, such as Mercury's "firehose" of magnetospheric cusp charged particles, galactic cosmic rays (GCR), solar energetic particles (SEP), and UV photons onto the polar ices, combined with gardening, overturn, sputtering and other physical processes in Mercury's surface materials should create ~centimeter-thick layers of dark refractory organics like those observed by instruments aboard the MESSENGER spacecraft.

References

Anand, M., Tartese, R., Barnes, J.J., 2014. Understanding the origin and evolution of water in the Moon through lunar sample studies. Phil. Trans. R. Soc. A. 372 art. 20130254, 33 pp.

Anderson, B.J., Johnson, C.L., Korth, H., et al., 2011. The global magnetic field of Mercury from MESSENGER orbital observations. Science 333, 1859–1862.

Baker, D.N., Odstrcil, D., Anderson, B.J., et al., 2011. The space environment of Mercury at the times of the second and third MESSENGER flybys. Planet. Space Sci. 59, 2066–2074.

Baratta, G.A., Fulvio, D., Garozzo, M., et al., 2012. Sulfur and carbon bearing molecules on the Galilean moons. Mem. S. A. It. Suppl. vol. 20, 94–98.

Benit, J., Bibring, J.P., Rocard, F., 1988. Chemical irradiation effects in ices. Nucl. Instrum. Methods Phys. Res., Sect. B 32, 349–353.

Benna, M., Anderson, B.J., Baker, D.N., et al., 2010. Modeling of the magnetosphere of Mercury at the time of the first MESSENGER flyby. Icarus 209, 3–10.

Bennett, C.J., Jamieson, C.S., Kaiser, R.I., 2008. Mechanistic studies on the decomposition of carbon suboxide in a cometary ice analog. Planet Space Sci. 56, 1181–1189.

Biver, N., Crovisier, J., Bockelee-Morvan, D., et al., 2012. Ammonia and other parent molecules in comet 10P/Tempel 2 from Herschel/HIFI and ground-based radio observations. Astron. Astrop. 539, A68, 6 pp. .

Black, G.J., Campbell, D.B., Harmon, J.K., 2010. Radar measurements of Mercury's north pole at 70 cm wavelength. Icarus 209, 224–229.

Blank, J.G., Miller, G.H., Ahrens, M.J., et al., 2001. Experimental shock chemistry of aqueous amino acid solutions and the cometary delivery of prebiotic compounds. Orig. Life Evol. Biosph 31 (1–2), 15–51.

Blank, J.G., 2009. Delivery of exogenous materials from comets and asteroids to the prebiotic Earth. Orig. Life Evol. Biosph. 39, 192–193.

Boduch, P., Dartois, E., de Barros, A.L.F., et al., 2015. Radiation effects in astrophysical ices. J. Phys. 629, 012008.

Botta, O., Bada, J.L., 2002a. Extraterrestrial organic compounds in meteorites. Surv. Geophys 23, 411–467.

Botta, O., Bada, J.L., 2002b. Extraterrestrial organic compounds in meteorites (vol 23, pg 411, 2002). Surv. Geophys. 23, 627.

Botta, O., Glavin, D.P., Kminek, G, et al., 2002. Relative amino acid concentrations as a signature for parent body processes of carbonaceous chondrites. Orig. Life Evol. Biospheres 32, 143–163.

Brown, W.L., Foti, G., Lanzerotti, L.J., et al., 1987. Delayed emission of hydrogen from ion bombardment of solid methane. Nucl. Instrum. Meth. B 19/20, 899–902.

Brown, M., Hill, R.E., 1996. Discovery of an extended sodium atmosphere around Europa. Nature 380, 229–231.

Bruck Syal, M., Schultz, P.H., Riner, M.A., 2013. Painting Mercury by comet-delivered carbon. 44th Lunar and Planetary Science Conference Abstracts #2496.

Burger, M.H., Killen, R.M., Vervack Jr., R.J., et al., 2010. Monte Carlo modeling of sodium in Mercury's exosphere during the first two MESSENGER flybys. Icarus 209, 63–74.

Butler, B.J., 1997. The migration of volatiles on the surfaces of Mercury and the Moon. J. Geophys. Res. 102, 19283–19292.

Chabot, N.L., Ernst, C.L., Denevi, B.W., et al., 2012. Areas of permanent shadow in Mercury's south polar region ascertained by MESSENGER orbital imaging. Geophys. Res. Lett. 39 art. L09204.

Chabot, N.L., Ernst, C.M., Denevi, B.W., et al., 2014. Images of surface volatiles in Mercury's polar craters acquired by the MESSENGER spacecraft. Geology 42, 1051–1054.

Chadderton, L.T., Torrens, I.M., 1969. Fission Damage in Crystals. Methuen, New York.

Chassefiere, E., Maria, J.L., Goutail, J.P., et al., 2010. PHEBUS: A double ultraviolet spectrometer to observe Mercury's exosphere. Planet. Space Sci. 58, 201–223.

Cheng, A.F., Lanzerotti, L.A., 1978. Ice sputtering by radiation belt protons and the rings of Saturn and Uranus. J. Geophys. Res. 83, 2597–2602.

Colaprete, A., Schultz, P., Heldmann, J., et al., 2010. Detection of water in the LCROSS ejecta plume. Science 330, 463–468.

Crawford, I.A., 2015. Lunar resources: A review. Prog. Phys. Geogr. 39, 137–167.

Cremonese, G., Warell, J., Harmon, J.K., et al., 2010. Techniques and methods in ground-based observation of Mercury. Planet. Space Sci. 58, 61–78.

Crites, S.T., Lucey, P.G., Lawrence, D.J., 2011. In-situ production of organic molecules at the poles of the Moon. AGU Meeting Abstract P13D-1730.

Crites, S.T., Lucey, P.G., Lawrence, D.J., 2013. Proton flux and radiation dose from galactic cosmic rays in the lunar regolith and implications for organic synthesis at the poles of the Moon and Mercury. Icarus 226, 1192–1200.

Cuzzi, J.N., Estrada, P.R., 1998. Compositional evolution of Saturn's rings due to meteoroid bombardment. Icarus 132, 1–35.

Dartnell, L.R., 2011. Ionizing radiation and life. Astrobiology 11 551-82 .

Dartois, E., Augé, B., Boduch, P., 2015. Heavy ion irradiation of crystalline water ice. Cosmic ray amorphisation cross-section and sputtering yield. Astron. Astrop. 576, A125.

Davis, D.R., Libby, W.F., Meinschein, W.G., 1966. Chemistry of positive ions. VI. Positive-Ion chemistry in solid methane. J. Chem. Phys. 45, 4481–4492.

Dawes, A., Hunniford, A., Holtom, P.D., et al., 2007. Low energy $^{13}C^+$ and $^{13}C^{2+}$ ion irradiation of water ice. Phys. Chem. Chem. Phys. 9, 2886–2893.

de Angelis, G., Badavi, F.F., Clem, J.M., et al., 2008. Modeling of the radiation environment on the Moon, Adv. Geosciences. In: Bhardwaj, A. (Ed.). Planetary Science, Vol. 19. World Scientific Publishing Company, New York.

Delitsky, M.L., Thompson, W.R., 1987. Chemical processes in Triton's atmosphere and surface. Icarus 70, 354–365.

Delitsky, M.L., Lane, A.L., 1997. Chemical schemes for surface modification of icy satellites: A road map. J. Geophys. Res. 102, 16385–16390.

Delitsky, M.L., Lane, A.L., 1998. Ice chemistry on the Galilean satellites. J. Geophys. Res. 103, 31391–31403.

Delitsky, M.L., Lane, A.L., 2002. Saturn's inner satellites: Ice chemistry and magnetosphere effects. J. Geophys. Res. 107 art. 5093.

Desai, M.I, Mason, G.M, Dayeh, M.A, et al., 2016. Spectral properties of large gradual solar energetic particle events. I. Fe, O, and seed material. Astrophys. J. 816 (68), 18pp.

Dewey, R.M., Baker, D.N., Slavin, J.A., et al., 2015. Intense energetic-electron flux enhancements in Mercury's magnetosphere: An integrated view with high-resolution observations from MESSENGER. AGU Fall Meeting Abstract P53A-2084.

Domingue, D.L., Koehn, P.L., Killen, R.M., et al., 2007. Mercury's atmosphere: A surface-bounded exosphere. Space Sci. Rev. 131, 161–186.

Domingue, D.L., Chapman, C.R., Killen, R.M., et al., 2014. Mercury's weather-beaten surface: Understanding Mercury in the context of lunar and asteroidal space weathering studies. Space Sci Rev. 181, 121–214.

Feldman, W.C., Maurice, S., Lawrence, D.J., et al., 2001. Evidence for water ice near the lunar poles. J. Geophys. Res. 106, 23,231–23,251.

Ferini, G., Baratta, G.A., Palumbo, M., 2004. A Raman study of ion irradiated icy mixtures. Astron. Astrop. 414, 757–766.

Foti, G., Calcagno, L., Sheng, K.L., et al., 1984. Micrometer-sized polymer layers synthesized by Mev ions impinging on frozen methane. Nature 310, 126–128.

Fridman, A., Gutsol, A., Dolgopolsky, A., et al., 2006. CO_2-free energy and hydrogen production from hydrocarbons. Energy Fuels 20, 1242–1249.

Frank, L.A., Sigwarth, J.B., Craven, J.D, 1986. Reply. Geophys. Res. Lett. 13, 703–704.

Geiger, R.P., 2013. Thesis. Plasmachemical Synthesis of Carbon Suboxide, Mechanical Engineering, Texas A&M University.

Geiger, R., Staack, D., 2011. Analysis of solid products formed in atmospheric non-thermal carbon monoxide plasma. J. Phys. D 44 (27).

Geiger, R., Staack, D., 2012. Non-thermal plasma-chemical CO_2 utilization: COx polymer formation. American Chemical Society Meeting, proceedings.
Gerakines, P.A., Moore, M.H., Hudson, R.L., 2000. Carbonic acid production in H_2O:CO_2 ices: UV photolysis vs. proton bombardment. Astron. Astrophys. 357, 793–800.
Gladstone, G.R., Retherford, K.D., Egan, A.F., et al., 2012. Far-ultraviolet reflectance properties of the Moon's permanently shadowed regions. J. Geophys. Res. 117, E00H04.
Harmon, J.K., Slade, M.A., Rice, M.S., 2011. Radar imagery of Mercury's putative polar ice: 1999–2005 Arecibo results. Icarus 211, 37–50.
Hayne, P.O., Hendrix, A.R., Sefton-Nash, E., et al., 2015. Evidence for exposed water ice in the Moon's south polar regions from Lunar Reconnaissance Orbiter ultraviolet albedo and temperature measurements. Icarus 255, 58–69.
Hendrix, A.R., Retherford, K.D., Gladstone, G.R., et al., 2012. The lunar far-UV albedo: Indicator of hydration and weathering. J. Geophys. Res. 117, E12001.
Ho, G.C., Krimigis, S.M., Gold, R.E., et al., 2011. MESSENGER observations of transient bursts of energetic electrons in Mercury's magnetosphere. Science 333, 1865–1868.
Ho, G.C., Krimigis, S.M., Gold, R.E., et al., 2016. MESSENGER observations of suprathermal electrons in Mercury's magnetosphere. Geophys. Res. Lett. 43, 550–555.
Hudson, R.L., Moore, M.H., 1995. Far-IR spectral changes accompanying proton irradiation of solids of astrochemical interest. Radiat. Phys. Chem. 45, 779–789.
Hudson, R.L., Moore, M.H., 1999. Laboratory studies of the formation of methanol and other organic molecules by water plus carbon monoxide radiolysis: Relevance to comets, icy satellites, and interstellar ices. Icarus 140, 451–461.
Hunniford, C.A., Dawes, A., Fulvio, D., et al., 2009. Irradiation of water ices by 2 keV carbon ions, 14th International conference on the physics of highly charged ions. J. Physics 163, 012078.
Huntress, W.T., Delitsky, M.L., 1988. Carbon suboxide in comet Halley? Bull. Amer. Astron. Soc. 20, 828.
Huntress, W.T., Allen, M.A., Delitsky, M.L., 1991. Carbon suboxide in Comet Halley? Nature 352, 316–318.
Hurley, D.M., Lawrence, D.J., Bussey, D.B.J., et al., 2012. Two-dimensional distribution of volatiles in the lunar regolith from space weathering simulations. Geophys. Res. Lett. 39, L09203.
Ishii, H.A., Bradley, J.P., Dai, Z.R., et al., 2008. Comparison of comet 81P/Wild 2 dust with interplanetary dust from comets. Science 329, 447–450.
Jamieson, C.S., Mebel, A.M., Kaiser, R.I., 2006. Understanding the kinetics and dynamics of radiation-induced reaction pathways in carbon monoxide ice at 10 K. Astrophys. J. Supp. Series 163, 184–206.
Jewitt, D., 2012. Lecture notes: http://www2.ess.ucla.edu/~jewitt/irradiation.html.
Jewitt, D., Chizmadia, L., Grimm, R., et al., 2007. Water in the small bodies of the solar system. In: Reipurth, V.B., Jewitt, D., Keil, K. (Eds.). In: Protostars and Planets V, 951. University of Arizona Press, Tucson, pp. 863–878.
Johnson, R.E., Cooper, J.F., Lanzerotti, L.J., et al., 1987. Radiation formation of a non-volatile comet crust. Astron. Astrop. 187, 889–892.
Johnson, R.E., 1990. Energetic Charged-Particle Interactions with Atmospheres and Surfaces. Springer, New York.
Johnson, R.E., 1991a. Irradiation effects in a comet's outer layers. J. Geophys. Res. 96, 17553–17557.
Johnson, R.E., 1991b. Irradiation of solids: Theory. In: Strazzula, G., Bussoletti, E. (Eds.), Solid-State Astrophysics Enrico Fermi Series, pp. 129–168.
Johnson, R.E., Carlson, R.W., Cooper, J.F., et al., 2004. Radiation effects on the surfaces of the Galilean satellites. In: Bagenal, F., Dowling, T.E., McKinnon, W.B. (Eds.), Jupiter: The planet, Satellites and Magnetosphere. Cambridge University Press.
Johnson, R.E., Carlson, R.W., Cassidy, T.A., et al., 2012. Sputtering of ices. In: Gudipati, M.S., Castillo-Rogez, J. (Eds.), The Science of Solar System Ices. Springer Science+Business Media, New York, p. 2012. ch. 17, Astrophysics and Space Science Library.
Jordan, A.P., Stubbs, T.J., Joyce, C.J., et al., 2013. The formation of molecular hydrogen from water ice in the lunar regolith by energetic charged particles. J. Geophys. Res. 118, 1257–1264.
Lane, A.L., Nelson, R.M., Matson, D.L., 1981. Evidence for sulphur implantation in Europa's UV absorption band. Nature 292, 38–39.
Lanzerotti, L.J., Brown, W.L., Maclennan, C.G., et al., 1987a. Effects of charged–particles on the surfaces of the satellites of Uranus. J. Geophys. Res. 92, 14949–14957.
Lanzerotti, L.J., Brown, W.L., Marcantonio, K.J., 1987b. Experimental study of erosion of methane ice by energetic ions and some considerations for astrophysics. Astrop. J. 313, 910–919.
Lawrence, D.J., Feldman, W.C., Goldsten, J.O., et al., 2013. Evidence for water ice near Mercury's north pole from MESSENGER neutron spectrometer measurements. Science 339, 292–296.
Liu, B.T., Lomov, I.N., Blank, J.G., et al., 2007. Simulation of comet impact and survivability of organic compounds. In: AIP Conf. Proc., 955, p. 1391.
Loeffler, M.J., Baragiola, R.A., 2009. Physical and chemical effects on crystalline H_2O_2 induced by 20 keV protons. J. Chem. Phys. 130, 114504.
Lucey, P., Neumann, G.A., Riner, M.A., et al., 2014. The global albedo of the Moon at 1064 nm from LOLA. J. Geophys. Res. 119, 1665–1679.
Lv, X.Y., de Barros, A.L.F., Boduch, P., et al., 2012. Implantation of multiply charged carbon ions in water ice. Astron. Astrop. 546, A81.
Matthews, C.N., Ludicky, R., 1986. The dark nucleus of Comet Halley: Hydrogen cyanide polymers. In: ESA Proceedings of the 20th ESLAB Symposium on the Exploration of Halley's Comet, 2, pp. 273–276. *Dust and Nucleus*.
McClintock, W.E., Bradley, E.T., Vervack, R.J., et al., 2008. Mercury's exosphere: Observations during MESSENGER's first Mercury flyby. Science 321, 92–94.
McClintock, W.E., Vervack Jr., R.J., Bradley, E.T., et al., 2009. MESSENGER observations of Mercury's exosphere: Detection of magnesium and distribution of constituents. Science 324, 610–613.
Meisels, G.G., Hamill, W.H., Williams, R.R., 1957. The radiation chemistry of methane. J. Phys. Chem. 61, 1456–1461.
Mejıa, C.F., de Barros, A.L.F., Bordalo, V., et al., 2013. Cosmic ray-ice interaction studied by radiolysis of 15 K methane ice with MeV O, Fe and Zn ions. MNRAS 433, 2368–2379.
Mewaldt, R.A., Cohen, C.M.S., Mason, G.M., et al., 2007. Long-term fluences of solar energetic particles from H to Fe. Space Sci. Rev. 130, 323–328.
Mishev, M., 2013. Short- and medium-term induced ionization in the Earth atmosphere by galactic and solar cosmic rays. Int. J. Atmos. Sci. art. ID 184508, 9 pp.
Mitchell, D.L., Lin, R.P., Carlson, C.W., et al., 1992. The origin of complex organic ions in the coma of Comet Halley. Icarus 98, 125–133.
Mouawad, N., Burger, M.H., Killen, R.M., et al., 2011. Constraints on Mercury's Na exosphere: Combined MESSENGER and ground-based data. Icarus 211, 21–36.
Mozumber, A., 1999. Fundamentals of Radiation Chemistry. Academic Press, New York.
Moore, M.H., Khanna, R.K., 1991. Infrared and mass-spectral studies of proton irradiated H_2O + CO_2 ice: Evidence for carbonic acid. Spectrochim Acta 47A, 255–262.
Moore, M.H., Khanna, R.K., Donn, B., 1991. Studies of proton irradiated H_2O + CO_2 and H_2O + CO ices and analysis of synthesized molecules. J. Geophys. Res. 96, 17541–17545.
Moses, J.L., Rawlins, K., Zahnle, K., et al., 1999. External sources of water for Mercury's putative ice deposits. Icarus 137, 197–221.
Mumma, M.J., Charnley, S.B., 2011. The chemical composition of comets—Emerging taxonomies and natal heritage. Ann. Rev. Astron. Astrop. 49, 471–524.
Ness, N.F., Behannon, K.W., Lepping, R.P., et al., 1974. Magnetic field observations near Mercury: Preliminary results from Mariner 10. Science 185, 151–160.
Ness, N.F., Behannon, K.W., Lepping, R.P., et al., 1975. Magnetic field of Mercury confirmed. Nature 255, 204–205.
Neumann, G.A., Cavanaugh, J.F., Sun, X., et al., 2013. Bright and dark polar deposits on Mercury: Evidence for surface volatiles. Science 339, 296–300.
Nozette, S., Spudis, P.D., Robinson, M.S., et al., 2001. Integration of lunar, polar remote sensing datasets: evidence for ice at the lunar south pole. J. Geophys Res. 106, 23253–23266.
Paige, D.A., Siegler, M.A., Zhang, J.A., et al., 2010. Diviner Lunar Radiometer Observations of cold traps in the Moon's south polar region. Science 330, 479–482.
Paige, D.A., Siegler, M.A., Harmon, J.K., et al., 2012. Thermal stability of frozen volatiles in the north polar region of Mercury. 43rd Lunar and Planetary Science Conference Abstract 2875.
Paige, D.A., Siegler, M.A., Harmon, J.K., et al., 2013. Thermal stability of volatiles in the north polar region of Mercury. Science 339, 300–303.
Paral, J., Trávníček, P.M., Rankin, R., et al., 2010. Sodium ion exosphere of Mercury during MESSENGER flybys. Geophys. Res. Lett. 37, L19102.
Paranicas, C., Cooper, J.F., Garrett, H.B., et al., 2009. Europa's radiation environment and its effects on the surface. In: Pappalardo, R.T., McKinnon, W.B., Khurana, K. (Eds.), Europa. University of Arizona Press, Tucson, AZ.
Peeters, Z., Hudson, R.L., Moore, M.H., et al., 2010. The formation and stability of carbonic acid on outer Solar System bodies. Icarus 210, 480–487.
Pilling, S., Nair, B.G., Escobar, A., et al., 2014. The temperature effect on the glycine decomposition induced by 2 keV electron bombardment in space analog conditions. Eur. Phys. J. D 68, 58.
Pryor, W.R., Holsclaw, G.M., McClintock, W.W., et al., 2013. Lyman-α Models for LRO LAMP from MESSENGER MASCS and SOHO SWAN Data, Cross-Calibration of Far UV Spectra of Solar System Objects and the Heliosphere. ISSI Scientific Report Series, Vol. 13, pp. 163–175.
Raines, J.M., Gershman, D.J., Zurbuchen, T.H., et al., 2013. Distribution and compositional variations of plasma ions in Mercury's space environment : The first three Mercury years of MESSENGER observations. J. Geophys. Res. 118, 1604–1619.
Raines, J.M., Gershman, D.J., Slavin, J.A., et al., 2014. Structure and dynamics of Mercury's magnetospheric cusp: MESSENGER measurements of protons and planetary ions. J. Geophys. Res. 119, 6587–6602.
Reitz, G., Berger, T., Matthiae, D.I., 2012. Radiation exposure in the moon environment. Planet. Space Sci. 74, 78–83.
Roessler, K., 1985a. Cosmic chemistry of carbon and nitrogen implants in ice. In: Origins and Early Evolution of Life (proceedings), Terra Cognita, 5, p. 128.
Roessler, K., 1985b. Hot atom chemistry and radiolysis of gaseous and solid components of planetary atmospheres. In: *The Atmospheres of Saturn and Titan*, Proceedings, ESA Spec. Publ. SP-241, pp. 175–188.
Roessler, K., 1986. Chemical modification of insulators by ion-implantation, Fundamental mechanisms and astrophysical implications, Radiat. Effects 99, 21–70.
Roessler, K., 1988. Hot atom chemistry in space -Simulation with nuclear methods. Radiochim. Acta 43, 123–125.
Roessler, K., 1992. Non-equilibrium chemistry in space. Nucl. Instrum. Methods Phys. Res., Sect. B 65, 55–66.
Roessler, K., Eich, G., 1988. Energy dependence of concentration of implants and its chemical consequences. Nucl. Instrum. Methods. Phys. Res., Sect. B 32, 446–452.
Roessler, K., Nebeling, B., 1987. Reactions of energetic carbon and nitrogen in H_2O, NH_3, and CH_4 ices and implications in cosmic chemistry. J. Phys. Paris 48 (C-1), 691.

Roessler, K., Nebeling, B., 1988. High energy and radiation chemistry in space, Lunar and Planetary Science conference, 1988, page 994, abstract #1503.
Roessler, K., Nebeling, B., Batista, M.C., 1985. Formation of organic compounds by impact of energetic atoms and ions on ice and frozen volatiles. Meteoritics 20, 748.
Ross, D.S., 2006. Cometary impact and amino acid survival–chemical kinetics and thermochemistry. J. Phys. Chem. A. 110, 6633–6637.
Rubin, M., Altwegg, K., Balsiger, H., et al., 2015. Molecular nitrogen in comet 67P/Churyumov-Gerasimenko indicates a low formation temperature. Science 348, 232–235.
Ruiz-Bermejo, M., Menor-Salván, C., Rogero, C., et al., 2009. HCN black polymers: A spectrometric/spectroscopic revision. Orig. Life Evol. Biosph. 39, 265.
Russell, C.T., 2000. The polar cusp. Adv. Space Res. 25, 1413–1424.
Sack, N., Johnson, R.E., Boring, J.W., et al., 1992. The effect of magnetospheric ion bombardment on the reflectance of Europa's surface. Icarus 100, 534–540.
Sagdeev, R.Z., Szabó, F., Avanesov, G.A., et al., 1986. Television observations of comet Halley from Vega spacecraft. Nature 321, 262–266.
Sarantos, M., Slavin, J.A., Benna, M., et al., 2009. Sodium-ion pickup observed above the magnetopause during MESSENGER's first Mercury flyby: Constraints on neutral exospheric models. Geophys. Res. Lett. 36, L04106.
Sarantos, M., Killen, R.M., McClintock, W.E., et al., 2011. Limits to Mercury's magnesium exosphere from MESSENGER second flyby observations. Planet. Space Sci 59, 1992–2003.
Schriver, D., Trávníček, P., Ashour-Abdalla, M., et al., 2011a. Electron transport and precipitation at Mercury during the MESSENGER flybys. Planet. Space Sci 59, 2026–2036.
Schriver, D., Trávníček, P.M., Anderson, B.J., et al., 2011b. Quasi-trapped particle population around Mercury. Geophys. Res. Lett. 38, L23103.
Schriver, D., Travnicek, P.M., Ho, G.C., et al., 2015. Energization and precipitation of electrons in Mercury's magnetosphere. AGU Meeting Abstract P53A-2089.
Schwadron, N.A., Baker, T., Blake, B., et al., 2012. Lunar radiation environment and space weathering from the cosmic ray telescope for the effects of radiation (CRaTER). J. Geophys. Res. 117, E00H13.
Scott, W.M., Wilson, H.W., 1968. A mass-spectrometric investigation of the radiolysis of methane by reactor radiation. Org. Mass Spectrom 1, 519–525.
Siegler, M.A., Bills, B.G., Paige, D.A., 2011. Effects of orbital evolution on lunar ice stability. J. Geophys. Res. 116 art no. E03010, 18 pp.
Siegler, M.A., Bills, B.G., Paige, D.A., 2013. Orbital eccentricity driven temperature variation at Mercury's pole. J. Geophys. Res. 118, 930–937.
Slade, M.A., Butler, B.J., Muhleman, D.O., 1992. Mercury radar imaging - evidence for polar ice. Science 258, 635–640.
Slavin, J.A., 2004. Mercury's magnetosphere. Adv. Space Res. 33, 1859–1874.
Slavin, J.A., Acuna, M.H., Anderson, B.J., et al., 2009. MESSENGER observations of magnetic reconnection in Mercury's magnetosphere. Science 324, 606–610.
Slavin, J.A., Anderson, B.J, Baker, D.N., et al., 2010a. MESSENGER observations of extreme loading and unloading of Mercury's magnetic tail. Science 329, 665–668.
Slavin, J.A., Lepping, R.P., Wu, C.-C., 2010b. MESSENGER observations of large flux transfer events at Mercury. Geophys. Res. Lett. 37, L02105.
Slavin, J.A., DiBraccio, G.A., Gershman, D.J., et al., 2014. MESSENGER observations of Mercury's dayside magnetosphere under extreme solar wind conditions. J. Geophys. Res. 119, 8087–8116.
Solomon, S.C., 2011. A new look at the planet Mercury. Physics Today 64, 50–55.
Spudis, P.D., Bussey, D.B.J., Baloga, S.M., et al., 2013. Evidence for water ice on the Moon: results for anomalous polar craters from the LRO Mini-RF imaging radar. J. Geophys. Res. 118, 2016–2029.
Starr, R.D., Schriver, D., Nittler, L.R., et al., 2012. MESSENGER detection of electron-induced x-ray fluorescence from Mercury's surface. J. Geophys. Res. 117, E00L02.
Stern, S.A., 2003. The evolution of comets in the Oort cloud and Kuiper belt. Nature 424, 639–642.
Stewart, B.D., Pierazzo, E., Goldstein, D.B, et al., 2011. Simulations of a comet impact on the Moon and associated ice deposition in polar cold traps. Icarus 215, 1–16.
Strazzulla, G., Calcagno, L., Foti, G., 1984a. Build up of carbonaceous material by fast protons on Pluto and Triton. Astron. Astrophys. 140, 441–444.
Strazzulla, G., Cataliotti, R.S., Calcagno, L., et al., 1984b. The IR spectrum of laboratory synthesized polymeric residues. Astron. Astrophys. 133, 77–79.
Strazzulla, G., Massimino, P., Spinella, F., et al., 1988. IR-spectra of irradiated organic materials. Infrared Phys. 28, 183–188.
Strazzulla, G., Johnson, R.E., 1991. Irradiation effects on comets and cometary debris. In: Comets in the Post-Halley Era, 1. Springer, New York, pp. 243–275.
Strazzulla, G., Baratta, G.A., Johnson, R.E., et al., 1991. Primordial comet mantle: Irradiation production of a stable organic crust. Icarus 91, 101–104.
Strazzulla, G., Baratta, G.A, 1992. Carbonaceous material by ion irradiation in space. Astron. Astrophys. 266, 434–438 http://adsabs.harvard.edu/full/1992A%26A...266..434S.
Strazzulla, G., 1997. Prebiotic chemistry induced by ion irradiation of ices. In: Chela-Flores, J., Raulin, F. (Eds.), *Exobiology: Matter, Energy, and Information in the Origin and Evolution of Life in the Universe*: Proceedings of the Fifth Trieste Conference on Chemical Evolution. Trieste, Italy , pp. 22–26. September 1997.
Strazzulla, G., Cooper, J.F., Christian, E.R., et al., 2003. Ion irradiation of TNOs: From the fluxes measured in space to the laboratory experiments. C.R. Physique 4, 791–801.
Strazzulla, G., Cooper, J.F., Christian, E.R., et al., 2011. Cosmic ion induced chemistry in ices. Rend. Fis. Acc. Lincei 22, 145–152.
Strazzulla, G., 2011. Cosmic ion bombardment of the icy moons of Jupiter. Nucl. Inst. Methods B. 269, 842–851.
Trávníček, P.M., Schriver, D., Hellinger, P., et al., 2010. Mercury's magnetosphere—solar wind interaction for northward and southward interplanetary magnetic field: Hybrid simulation results. Icarus 209, 11–22.
Tripathi, R.K., Wilson, J.W., Badavi, F.F., et al., 2006. A characterization of the moon radiation environment for radiation analysis. Adv. Space Res 37, 1749–1758.
Usoskin, I.G., Kovaltsov, G.A., 2012. Occurrence of extreme solar particle events: Assessment from historical proxy data. Astrophys. J. 757, 92 6 pp.
Watson, K, Murray, B.C., Brown, H., 1963. The stability of volatiles in the solar system. Icarus 1, 317–327.
Webber, W.R., Higbie, P.R., McCracken, K.G., 2007. Production of the cosmogenic isotopes ^{3}H, ^{7}Be, ^{10}Be, and ^{36}Cl in the Earth's atmosphere by solar and galactic cosmic rays. J. Geophys. Res. 112, A10106.
Winslow, R.M., Johnson, C.L., Anderson, B.J., et al., 2012. Observations of Mercury's northern cusp region with MESSENGER's magnetometer. Geophys. Res. Lett. 39, L08112.
Wyckoff, S., Tegler, S.C., Engel, L., 1991. Ammonia abundances in four comets. Astrophys. J. 368, 279–286.
Zhang, J.A., Paige, D.A., 2009. Cold-trapped organic compounds at the poles of the Moon and Mercury: Implications for origins. Geophys. Res. Lett 36, L16203.
Zhang, J., Paige, D.A., 2010. Correction to "Cold-trapped organic compounds at the poles of the Moon and Mercury: Implications for origins. Geophys. Res. Lett. 37, L03203 http://onlinelibrary.wiley.com/doi/10.1029/2009GL041806/pdf.
Zurbuchen, T.H., Raines, J.M., Gloeckler, G., et al., 2008. MESSENGER observations of the composition of Mercury's ionized exosphere and plasma environment. Science 321, 90–92.
Zurbuchen, T.H., Raines, J.M., Slavin, J.A., et al., 2011. MESSENGER observations of the spatial distribution of planetary ions near Mercury. Science 333, 1862–1865.